Centennial- to millennial-scale hard rock erosion rates deduced from luminescence-depth profiles

Reza Sohbati
Jinfeng Liu
Mayank Jain
Andrew Murray
David Egholm
Richard Paris
Benny Guralnik

The published article is available from doi:
http://dx.doi.org/10.1016/j.epsl.2018.04.017

Centennial- to millennial-scale hard rock erosion rates deduced from luminescence-depth profiles

Reza Sohbati[a,b], Jinfeng Liu[c,*], Mayank Jain[a], Andrew Murray[b], David Egholm[d], Richard Paris[e], Benny Guralnik[b,f]

[a]Center for Nuclear Technologies, Technical University of Denmark, DK 4000 Roskilde, Denmark
[b]The Nordic Laboratory for Luminescence Dating, Department of Geoscience, Aarhus University, DK 4000 Roskilde, Denmark
[c]State Key Laboratory of Earthquake Dynamics, Institute of Geology, China Earthquake Administration, China
[d]Department of Geoscience, Aarhus University, 8000 Aarhus, Denmark
[e]Department of Computing and Mathematics, University of Abertay, Dundee DD1 1HG, UK
[f]Soil Geography and Landscape group and the Netherlands Centre for Luminescence Dating, Wageningen University, Droevendaalsesteeg 3, 6708PB Wageningen, The Netherlands

*Corresponding author: liujf81@ies.ac.cn

Abstract

The measurement of erosion and weathering rates in different geomorphic settings and over diverse temporal and spatial scales is fundamental to the quantification of rates and patterns of earth surface processes. A knowledge of the rates of these surface processes helps one to decipher their relative contribution to landscape evolution – information that is crucial to understanding the interaction between climate, tectonics and landscape. Consequently, a wide range of techniques has been developed to determine short- ($<10^2$ a) and long-term ($> 10^4$ a) erosion rates. However, no method is available to quantify hard rock erosion rates at centennial to millennial timescales. Here we propose a novel technique, based on the solar bleaching of luminescence signals with depth into rock surfaces, to bridge this analytical gap. We apply our technique to glacial and landslide boulders in the Eastern Pamirs, China. The calculated erosion rates from the smooth varnished surfaces of 7 out of the 8 boulders sampled in this study vary between < 0.038±0.002 and 1.72±0.04 mm ka^{-1} (the eighth boulder gave an anomalously high erosion rate, possibly due to a recent chipping/cracking loss of surface). Given this preferential sampling of smooth surfaces, assumed to arise from grain-by-grain surface loss, we consider these rates as minimum estimates of rock surface denudation rates in the Eastern Pamirs, China.

1. Introduction

The erosion of the Earth's surface results from a combination of physical, chemical and biological weathering and the subsequent removal of weathering products by various transport agents. Erosion of rock surfaces may result from a range of processes such as dissolution, grain-by-grain attrition, chipping/frost cracking, and even massive bedrock landslides. Quantifying the rates and timing of such processes over various spatial and temporal scales is fundamental to determining the relative contribution of each process and thereby understanding landscape evolution. Bare hard rock surfaces are the most durable surficial features in the landscape and thus can have a long memory of the erosional history. Consequently, a wide range of methods have been developed to quantify erosion rates of subaerially-exposed rock surfaces (Turkowski and Cook, 2017). These include: i) the direct/indirect measurement of surface loss over laboratory timescales, or by comparison with resistant natural or anthropogenic reference features of known-age (Stephenson and Finlayson, 2009; Moses et al., 2014), ii) the analysis of cosmogenic nuclides (CNs) produced within mineral grains from exposed rock surfaces as a result of bombardment by secondary cosmic rays (Nishizumi et al., 1986; Lal, 1991), and iii) thermochronology using a wide range of radiogenic processes to determine the thermal history of rocks, and thus their exhumation rates (Braun et al., 2006). Depending on the length of the observation period or the age of the reference feature, the rates measured by the techniques in category (i) are integrated over sub-annual to multi-decadal timescales (Moses et al., 2014), while the rates derived using CNs and thermochronology are averaged over thousands to millions of years, respectively (Lal, 1991, Braun et al., 2006). The short (i.e. $< 10^2$ years) and long (i.e. $> 10^4$ years) timescales of these techniques leave an intermediate time interval of 10^2–10^4 years over which there is currently no technique available for quantifying the erosion rates of rock surfaces. The centennial to millennial time intervals are of particular importance and interest to human society for evaluating the effects of climate change or anthropogenic activity on landscape evolution.

One of the major challenges in geomorphology is to make a link between different scales of observation (Schumm and Litchy, 1965; Warke and McKinley, 2011). Specifically, the timescale over which the rates of earth surface processes are averaged directly influences the apparent rates (e.g. Gardner et al., 1987; Viles, 2001; Koppes and Montgomery, 2009). Such measurement-interval bias can result in either underestimation (e.g. Kirchner et al., 2001) or overestimation (e.g. Lal et al., 2005) of short-term measurements compared to long-term average rates, hindering a linkage by simple extrapolation between the rates averaged over timescales that are orders of magnitude different (Gardner et al., 1987). It is clear that the development of a new analytical tool to bridge the gap between the decadal and millennial timescales would be of considerable value in erosion studies.

Several studies have shown that when a rock surface is first exposed to daylight, the latent luminescence, mainly from the constituent minerals quartz and feldspar, starts to decrease. The rate of this resetting (or 'bleaching') process decreases with depth as the incident light is attenuated (e.g. Habermann et al., 2000; Laskaris and Liritzis, 2011). Based on this phenomenon, Sohbati et al. (2011, 2012a,b) proposed a new surface-exposure dating technique, which utilizes the time and depth dependence of the residual latent luminescence. The longer the rock is exposed to daylight, the deeper is the transition zone between the region of bleached latent luminescence at the surface and saturated latent luminescence at depth. After calibration, the depth of this "optical bleaching front" can be translated to an exposure time (Sohbati et al., 2011, 2012a,b).

CN-depth profiles are influenced by the effect of erosion; Lal (1991) points out that the rock depth equivalent to one absorption mean free path for cosmic rays is ~50 cm. In contrast, the corresponding absorption mean free path for light penetration into rocks is on the scale of millimetres (Sohbati et al., 2011, 2012a,b). Thus, luminescence-depth profiles are expected to be ~2 orders of magnitude more sensitive to the effect of erosion. In contrast to the effect of daylight exposure, the transition zone between the surface bleached latent luminescence and the saturated latent luminescence will become shallower, the higher the erosion rate. Nevertheless, this effect has been considered to be unimportant in all published applications, because the technique was applied to surfaces where archaeological evidence suggested negligible erosion (e.g. Pederson et al., 2014). However, the application of the technique to geological features, where constraints on surface preservation are rare on the centimetre scale (Lehmann et al., 2018 being an exception), necessitates the effect of erosion be taken into account (Sanderson et al., 2011). Here, we present a further development of the luminescence surface-exposure dating model (Sohbati et al., 2012b) that includes the effect of erosion on luminescence-depth profiles. We then use the new model to derive steady-state centennial- to millennial-scale hard-rock erosion rates from several surface-exposed glacial and landslide boulders from the Pamir plateau, China.

2. Theoretical framework

The ubiquitous rock-forming minerals quartz and feldspar can store energy (in the form of trapped charge) through the absorption of ionizing radiation resulting from the decay of naturally-occurring radionuclides (mainly ^{238}U and ^{232}Th and their decay products, and ^{40}K) and cosmic rays. This trapped charge can be released during exposure to heat or light. Some of the energy released during the resetting is emitted as photons (i.e. as UV, visible, or near infrared luminescence); if the trapped charge is released by light (i.e. photon stimulation of trapped electrons), the luminescence emitted from the mineral is called optically stimulated luminescence (OSL; Aitken, 1998). OSL is now a well-established Quaternary dating method usually used to determine the time elapsed since mineral grains were last exposed to daylight (i.e. the burial age) (Aitken, 1998). Recently, luminescence has also been shown to be useful in surface exposure dating (Sohbati et al., 2012a, b).

2.1. Luminescence surface exposure age

In any rock sample that has been deeply buried and therefore shielded from light for an extended length of time (typically > 0.5 Ma) the trapped electron population in the constituent quartz and feldspar crystals will usually be in field saturation due to finite trapping capacity (e.g. Guralnik et al., 2013). If the rock is then exposed to daylight by an exhumation event (e.g. fracture, ice-scouring) the trapped electron population will begin to decrease. The electron detrapping rate decreases with depth as a result of the attenuation of incident light with depth, following Beer-Lambert law (e.g. Laskaris and Liritzis, 2011). The rate of change of trapped electron population at a particular depth is a result of competition between two effects: (i) the accumulation rate of trapped electrons due to ambient ionizing radiation, and (ii) the eviction rate of trapped electrons due to the daylight flux at a given depth. Thus, in a rock that has been exposed to daylight, the residual luminescence forms a sigmoidal profile that continues to evolve with time until it reaches secular equilibrium, when electron trapping and detrapping rates are equal at all depths (Fig. 1a). For a given exposure time and daylight conditions, the penetration depth and form of a luminescence profile depend on the opacity of the rock-forming minerals and the relevant photoionization cross section(s). Assuming that luminescence signal is proportional to the trapped electron population, Sohbati et al. (2011, 2012a, b) developed a mathematical model describing the luminescence-depth profiles in rock surfaces and demonstrated its application in surface exposure dating. According to this model, which assumes first-order kinetics for electron trapping and detrapping, the instantaneous concentration of trapped electrons n (mm^{-3}) at a depth of x (mm) can be expressed as:

$$\frac{dn}{dt} = (N - n)F(x) \; - nE(x) \qquad (1)$$

where t (ka) is time, N (mm^{-3}) is the concentration of electron traps, and $F(x)$ and $E(x)$ (both ka^{-1}) are the rate constants describing electron trap filling and emptying, respectively.

$E(x)$ (ka^{-1}) decreases with depth due to attenuation of daylight intensity into the rock following the Beer-Lambert law:

$$E(x) = \overline{\sigma\varphi_0} e^{-\mu x} \qquad (2)$$

where $\overline{\sigma\varphi_0}$ (ka^{-1}) is the time-averaged detrapping rate constant at the surface of the rock and μ (mm^{-1}) is the inverse of the mean free path of photons in the rock.

The coefficient $F(x)$ describes the trapping rate constant:

$$F(x) = \dot{D}(x)/\, D_0 \qquad (3)$$

where $\dot{D}$ (Gy ka^{-1}) is the natural dose rate and D_0(Gy) is the characteristic dose that fills ~63% (i.e. $1 - e^{-1}$) of the traps (Wintle and Murray, 2006). D_0 is an intrinsic property of the dosimeter and not expected to have any systematic dependence on depth. $\dot{D}$ may have a weak dependence on depth into the rock, especially close to the surface (e.g. Sohbati et al., 2015) due to short range of the beta particles, but this can be neglected for exposure dating, since near the surface, $E(x)$ exceeds $F(x)$ by many orders of magnitude. Thus, in the present context, the dose rate may well be approximated as a depth-independent constant, i.e. $F(x) \approx F = const$.

When a previously shielded rock is first exposed to light, the initial trapped electron population $n_0 \cong N$, assuming a stable trapped electron population. Solving Eqn. (1) with the boundary condition of $n = N$ at $t = 0$ yields:

$$\frac{n(x,t)}{N} = \frac{E(x)e^{-t[E(x)+F]} + F}{E(x) + F} \qquad (4)$$

According to this model, as the exposure time increases, the luminescence profile advances further into the rock until $dn/dt \cong 0$ at all depths (Fig. 1a). In the absence of erosion (i.e. with a time-invariant x), the model can be used to derive exposure ages as old as 100 ka, depending on the values of the model parameters (Sohbati et al., 2012a, b) (Fig. 1a).

The millimetre depth scale of the luminescence resetting profiles, however, make them highly susceptible to the effect of erosion (i.e. x decreases with time). In any case, the assumption of zero erosion is far from true for most terrestrial surfaces (e.g. Portenga and Bierman, 2011). Any exfoliation of the rock surface and/or removal of bleached material from the surface due to weathering and erosion moves the luminescence profile closer to the surface, preventing the derivation of a simple exposure age. Below, we explore the effect of erosion on luminescence-depth profiles with the aim of deriving erosion rates from such data.

2.2. Luminescence steady-state erosion rate

The spatially-uniform removal of the uppermost material from a column of rock at a steady rate ε (mm ka^{-1}), affects the depth of all underlying material as follows:

$$\frac{dx}{dt} = -\varepsilon \tag{5}$$

where $\varepsilon \geq 0$. Eqn. (5) can be integrated with regard to time to yield $x(t) = x_0 - \varepsilon t$, where x_0 is an arbitrary depth datum. Substitution of a time-dependent depth $x(t)$ from Eqn. (5) into the electron detrapping rate constant $E(x)$ (Eqn. 2) results in:

$$E(x(t)) = \overline{\sigma\varphi_0} e^{-\mu(x_0 - \varepsilon t)} = (\overline{\sigma\varphi_0} e^{-\mu x_0}) e^{\mu\varepsilon t} = E_0 e^{\mu\varepsilon t} \tag{6}$$

where $E_0 = \overline{\sigma\varphi_0} e^{-\mu x_0}$ is the trap emptying rate constant at x_0. The substitution of Eqn. (6) into Eqn. (1) yields:

$$\frac{dn}{dt} = (N - n)F - nE_0 e^{\mu\varepsilon t} \tag{7}$$

which is functionally identical to the description of a luminescence-thermochronometer (Guralnik et al., 2013), except for the sign within the exponential. This subtle difference, i.e. the trap emptying rate increases (rather than diminishes) with time, leads to a substantially different solution for n (Appendix A). To describe steady-state erosion, we define the datum depth to be infinitely deep (i.e. $x_0 = \infty$) (Lal, 1991), and obtain an analytical solution for Eqn. (7):

$$\frac{n(x,\varepsilon)}{N} = M\left(1, 1 + \frac{F}{\mu\varepsilon}, -\frac{E(x)}{\mu\varepsilon}\right) \tag{8}$$

where M is the confluent hypergeometric function (Abramowitz and Stegun, 1964), readily available in the majority of common computing software (Appendix A). Eqn. (8) describes the luminescence-depth profile in a rock surface that has been continuously eroding at a rate ε (mm ka^{-1}) (Fig. 1b).

A luminescence-depth profile can be interpreted either in terms of an apparent exposure age (Eqn. 4) or an apparent steady-state erosion rate (Eqn. 8). As in CN dating, in the absence of other information one cannot choose between the two interpretations (Lal, 1991); an independent constraint on age or erosion rate is required to identify which model to select and so derive the true erosion rate or age, respectively. Provided that all other model parameters (i.e. $\dot{D}$, D_0, μ, and $\overline{\sigma\varphi_0}$) are quantified, the exposure age (t) or erosion rate (ε) can be derived from an observed luminescence-depth profile via fitting of Eqns. (4) or (8), respectively.

In practice, there is a limit to how well a profile can be distinguished from a profile in secular equilibrium. Any luminescence-depth profile can be characterized by the depth $x_{50\%}$, at which the signal intensity drops to 50% of that in saturation (at depth). In a steady-state profile, this depth $x_{50\%,SS}$ can be easily predicted from Eq. (4) (when $t \rightarrow \infty$). Here, we make a conservative assumption that a depth difference of at least one mean free path (i.e. $1/\mu$) is required to experimentally distinguish a transient profile from a predicted steady-state profile. This means the apparent exposure age or erosion rate of any profile whose ($x_{50\%} > x_{50\%,SS} - 1/\mu$) should be considered as apparent minimum age or maximum erosion rate, respectively.

We now test both the luminescence surface exposure and erosion rate models by applying them to several glacial and landslide boulders in the Eastern Pamirs, China. The surface exposure ages of all these boulders have been previously established using ^{10}Be dating.

3. Study area and sampling sites

The Tashkurgan Valley stretches NNW for ~100 km along the trace of the Karakoram and Tashkurgan faults, marking the junction between the Karakoram, Pamir and Western Tibet (Fig. 2). The valley floor contains many landslide and glacial erratic boulders whose chronology can provide valuable information about the driving mechanisms such as enhanced earthquake activity and climate change (Owen et al., 2012; Yuan et al., 2013). As a result, the area has been subject to extensive research in recent years, mostly based on CN surface exposure dating of boulders. Tens of glacial and landslide boulders have been dated using ^{10}Be by various workers (e.g. Seong et al., 2009a,b,c; Owen et al., 2012; Yuan et al., 2013; Xu and Yi, 2014), providing an excellent independent-age control dataset for our model verification.

At different locations along the valley, we visited three sites previously studied by others (Seong et al., 2009a; Owen et al., 2012; Yuan et al., 2013) (Fig. 2). These locations were selected based on (i) well-constrained chronology as shown by converging ^{10}Be ages obtained from several (> 6) boulders at each site, and (ii) ages covering a wide range of 7 to 70 ka (Fig. 2). We sampled the flat tops of large boulders (> 2 m in diameter) close to the points previously sampled for CN dating, as well as the exposed surfaces of a few smaller boulders (<1 m in diameter) close to the large boulders (Fig. 3). These were most likely deposited at the same time as the large boulders, but they are usually dismissed in CN studies, mainly because of concerns related to post-depositional reworking. Boulder surfaces varied from being smooth, visually homogenous with various degrees of desert varnish to more sporadic cm-scale exfoliation (Figs. 3 and 4). Sub-mm- to mm-scale weathering and grain loss was evidenced by friable surfaces from which individual grains could be readily removed by light mechanical abrasion (rubbing by hand). Samples were collected from surfaces with abundant desert varnish, where we assume chipping is probably a less important surface removal mechanism.

4. Methods

4.1. Sampling and sample preparation

Blocks of ~4×4×7 cm^3 were cut from the boulder surfaces using a petrol-driven cut-off saw equipped with a dry-cut diamond blade (Fig. 3). Blocks were immediately wrapped in aluminium foil and light-tight plastic bags to avoid any further exposure to daylight after collection. Under subdued red-orange light in the laboratory, cores 10 mm in diameter and up to 50 mm long were drilled into blocks using a water-cooled diamond core drill; these cores were then cut into 1.2 mm thick slices using a water-cooled low-speed saw equipped with a 0.3 mm thick diamond wafer blade, giving a net slice spacing of 1.5 mm. The outermost slices were treated by 10% HF for 40 min. and 10% HCl for 20 min. to remove any weathering products. No treatment was given to inner slices (Sohbati et al., 2011).

A subsample of ~150 g was also prepared from each sample for dose rate measurement. These were pulverized, homogenized and then cast in wax to prevent radon loss and to provide a reproducible counting geometry. They were then stored for at least three weeks to allow ^{222}Rn to reach equilibrium with its parent ^{226}Ra before the measurement.

4.2. Analytical facilities and measurements

Although quartz OSL is usually the preferred signal in sediment dating, it is often not sufficiently sensitive when measured in primary rocks (e.g. Sohbati et al., 2011; Guralnik et al., 2015). Thus, we made use of infrared stimulated luminescence (IRSL) signal to measure the solid rock slices. The IRSL signal originates almost entirely from feldspar grains in rock slices (e.g. Baril and Huntley, 2003).

Luminescence measurements were carried out using a Risø TL/OSL reader (model DA-20) with infrared light stimulation (870 nm, ~130 mW cm^{-2}) and photon detection through a Schott BG 39/Corning 7-59 blue filter combination (2 and 4 mm, respectively). Beta irradiations used a calibrated

$^{90}Sr/^{90}Y$ source mounted on the reader delivering a dose rate of ~0.08 Gy s^{-1} to the rock slices. The IRSL signal was measured using a conventional single-aliquot regenerative-dose (SAR) protocol. The residual natural signal (L_n) and the subsequent response to a test dose (T_n) from each slice were measured using an IRSL signal at 50°C (IR_{50}) for 100 s (Wallinga et al., 2000). A pause of 30 s was inserted before the stimulation to make sure that all the grains within a slice reached the stimulation temperature. The same thermal pretreatment of 250°C for 100 s was applied before the natural and test dose measurements. Each cycle of the SAR protocol finished with an IR stimulation at 290°C for 100 s to minimize recuperation (Wallinga et al., 2007).

The radionuclide concentrations (^{238}U, ^{226}Ra, ^{232}Th and ^{40}K) were determined using high-resolution gamma spectrometry by measurement on a high-purity germanium detector for at least 24 h. Details of the gamma spectrometry calibration are given in Murray et al. (1987). To calculate the size-dependent internal beta dose rate from ^{40}K in K-rich feldspar grains, a grain size and composition analysis was carried out, using scanning electron microscopy (SEM), on several slices from each rock to determine the average size of the constituent K-rich feldspar grains (Table 1S). Using the simplifying assumption that the grains are spherical with this dimension as the diameter, the beta dose rate contributions from ^{40}K and ^{87}Rb were then calculated assuming a potassium content of 12.5± 0.5% (Huntley and Baril, 1997) and a ^{87}Rb content of 400 ± 100 ppm (Huntley and Hancock, 2001). A small internal alpha contribution of 0.10 ± 0.05 Gy ka^{-1} from internal ^{238}U and ^{232}Th was also included in the dose rates, derived from ^{238}U and ^{232}Th concentration measurements by Mejdahl (1987). The radionuclide concentrations were converted to dose rate data using the conversion factors from Guérin et al. (2011). The contribution from cosmic radiation to the dose rate was calculated following Prescott and Hutton (1994), assuming an uncertainty of 5%. The water content is negligible. Radionuclide concentrations and infinite-matrix beta and gamma dose rates are summarized in Table S1.

5. Results

5.1. Estimation of model parameters

To derive the exposure age (t) (Eqn. 4) or the erosion rate (ε) (Eqn. 8) by fitting the corresponding equations to luminescence-depth profiles, the values of other parameters in the models must be derived independently. This can be done either by derivation from first principles or by fitting the models to an appropriate calibration sample (Sohbati et al., 2011, 2012a, b). We next discuss the evaluation of the individual parameters:

Dose rate ($\dot{D}$): Ideally, in order for the beta and gamma dose rates derived from gamma spectrometry to be applicable to the IRSL-depth profiles, they need to be modified to account for the deviation from the infinite-matrix assumption around the rock surface-air interface. However, as mentioned before, this is not relevant to our problem. In practice, the average linear beta attenuation coefficient in granitic rocks with a typical density of ~2.6 g.cm^{-3} is ~1.9 mm^{-1} (e.g. Sohbati et al., 2015). Hence the beta dose rate reaches ~98% of the infinite matrix dose rate at a depth of ~2 mm in our samples. Given that electron detrapping rate due to daylight bleaching at such depths (i.e. < 2 mm) is much higher than electron trapping rate by dose rate, the effect of beta dose rate variation in the bleached part of the profile is negligible. The gradient of gamma dose rate with depth, on the other hand, is much less steep than that of beta (e.g. Aitken, 1985) and occurs over the entire length of the profiles measured here (i.e. ~3.5 cm). The gamma linear attenuation coefficient was calculated following Sohbati et al. (2015). The calculated coefficient is ~0.02 mm^{-1}, which results in an increase of gamma dose rate by a factor of ~1.5 from the surface to a depth of ~3.5 cm; however, on average, the gamma dose rate is only ~30% of the total dose rate in our samples. Thus, there is only a weak variation of total dose rate with depth, which may be neglected for the benefit of simplification of the model. The variation of cosmic dose rate due to the attenuation of cosmic rays into rocks was also calculated using the depth dependence model of Prescott and Hutton (1994). The resulting beta (including contributions from internal ^{40}K and ^{87}Rb), gamma and cosmic dose rates were then summed and averaged over the length of each luminescence-depth profile to give the mean effective total dose rate in Eqns. (4) and (8) (Table 1).

Characteristic dose (D_0): To estimate the value of D_0 for each boulder, the dose-response curves of the surface and the deepest slice from one of the luminescence-depth profiles for each sample, were measured up to high doses (up to ~1000 Gy, i.e. close to saturation). The resulting dose-response curves were then fitted with a single saturating exponential function to calculate the value of D_0. Although the resulting D_0 values vary significantly from sample to sample, no systematic difference with depth within individual samples is observed. We therefore take an average of the two D_0 values for each sample as the most representative value to be used in Eqns. (4) and (11) for the whole profile (Table 1).

Luminescence decay rate ($\overline{\sigma\varphi_0}$) *and light attenuation coefficient* (μ): As shown in Eqn. 2, the overall rate of charge detrapping $E(x)$ (ka^{-1}) (Eqn. 2) is a function of charge detrapping rate at the surface of the rock $\overline{\sigma\varphi_0}$ (ka^{-1}) and the linear light attenuation coefficient μ (mm^{-1}) into the rock. These site-specific and material-dependent parameters can, in principle, be determined independently from first principles and/or by controlled field and laboratory measurements. However, earlier theoretically-derived values of $\overline{\sigma\varphi_0}$ have been shown to be orders of magnitude different from the empirically-derived values obtained by regression of the model to known-age calibration samples (Sohbati et al., 2011; 2012a), and no attempt to measure μ in the laboratory has been reported. The alternative empirical approach is to quantify these parameters by fitting the model to a non-eroding known-age calibration sample (Sohbati et al., 2012a). Such a surface was serendipitously created in one location by earlier workers collecting CN samples during an earlier field campaign in 2010 (sampling date given by Zhaode Yuan, personal communication) (Fig. 4). Fresh chisel marks on the surface of the boulder provide evidence that the surface has not eroded significantly during the known exposure period (~3 years). We sampled two profiles within a few centimeters of each other; one was taken from the natural surface of the boulder, complete with varnish, and a second from the bottom of a > 2-cm deep chiseled surface (Fig. 4). A simple qualitative assessment shows that the signal resetting in the profile from the original surface with a ^{10}Be age of 15.7 ka penetrates further into the rock than that in the core from the > 2-cm deep chisel mark (Fig. 4). This is in line with the prediction of the model that luminescence is reset deeper into the surface with longer exposure time. A further comparison between the two profiles shows that the piece removed in 2010 was almost certainly thick enough (> 2 cm) to eliminate the part of the profile that was bleached prior to CN sampling (i.e. < 2 cm, Fig. 4). We can thus be confident that the present-day shallow profile was saturated at the surface as a result of sampling three years ago (satisfying the condition of $n = N$ at the beginning of the bleaching–irradiation process, $t = 0$) and has not undergone any significant erosion during this period.

A visual inspection of the resetting fronts in the two profiles also reveals that they have similar curvature (Fig. 4; see also Fig. S1). According to the model, the gradient of luminescence-depth profiles is controlled by the attenuation of light into the surface (μ in Eqn. 2). Given the material-dependent nature of this parameter and the similarity of the curvature of the two profiles, we assume that they have the same light attenuation coefficient (Fig. 4).

We fit the two datasets simultaneously by sharing $\overline{\sigma\varphi_0}$ and μ between the profiles and replacing the length of exposure time t by three years in the model for the shallow profile. The 3-year old profile is our reference data for calibration; it allows us to determine the values of the model parameters, and thereby, the apparent exposure time for the deeper profile (Figs. 4 and 5c). The best-fit values for $\overline{\sigma\varphi_0}$ and μ are 2165±51 ka^{-1} and 0.59±0.01 mm^{-1}, respectively. The apparent best-fit luminescence surface-exposure age for the deeper profile is 2.5±0.3 ka, much younger than the ^{10}Be exposure age of 15.7 ka obtained from the same surface. This obvious age underestimation is presumed to arise from the effect of erosion on the luminescence-depth profile. Using the best-fit values for $\overline{\sigma\varphi_0}$ and μ and setting the exposure time t to 15.7 ka results in a predicted luminescence profile that penetrates much deeper than that measured (Figs. 4 and 5c). This is the profile that would have developed in 15.7 ka, had there been no erosion. Similarly, we can model the secular-equilibrium profile ($dn/dt = 0$) for zero erosion rate (Figs. 4 and 5c); it penetrates even deeper than the 15.7 ka profile. All three profiles are statistically distinguishable suggesting that in the absence of erosion a 15.7 ka profile could have been resolved from the secular-equilibrium profile.

5.2. The effect of feldspar IRSL signal instability on the models

Our models implicitly assume that the competition between electron trap filling by environmental radiation and trap emptying by optical bleaching in IRSL-depth profiles is governed by first-order kinetics. However, trapped electrons participating in IRSL often undergo localized recombination from the ground state and/or the excited state of the trap leading to signal instability (e.g., Huntley, 2006; Jain et al., 2015). Such a signal instability is expected to affect the shape of the luminescence-depth profile because recently-trapped charge (i.e. charge population far from field equilibrium; Lamothe et al., 2003) makes up a larger fraction of the total at low signal intensities (i.e. shallower depths) than at high signal intensities closer to saturation (i.e. deeper in the profile). Nonetheless, for our samples we assume we can ignore these effects in a first order approximation, because the apparent luminescence ages (discussed below) are, with one exception, < 12 ka. On such timescales, any second order effects related to instability of the signal acquired due to ambient ionizing radiation is negligible compared to bleaching by daylight close to the surface.

To test the validity of this approximation, we have superimposed the bleaching profiles from the 3-year old calibration sample (Fig. 4, profile 1) with the profile from the adjacent natural surface presumed to have been exposed for 15.7 ka (^{10}Be age; Fig. 4, profile 2), by simply adding 12 mm to the depth scale of the 3-year old profile (see Fig. S1). The two profiles are now indistinguishable, confirming that any effect of signal instability on the shape of the profile is negligible over a timescale of up to ~16 ka.

5.3. Apparent ages and erosion rates

As presented earlier, we have two explicit models represented by two different analytical solutions: the age model (Eqn. 4; assumes no erosion and solves for exposure age) and the steady-state erosion rate model (Eqn. 8, assumes no age information and solves for erosion rate). In this section, we first apply the age model to all the luminescence-depth profiles and then the erosion rate model.

Figure 5 shows the IRSL-depth profiles measured into the 8 boulder surfaces. All the profiles have the characteristic sigmoidal shape as predicted by the model for constantly exposed surfaces; they start at negligible values at the surface and gently rise to saturation at depths > 20 mm. Given that all the samples were collected from the top flat surfaces of boulders from localities that are < 100 km apart within the valley, we assume that they have all been exposed to similar solar insolation (φ_0). Also, it has been shown that feldspars of different compositions have similar bleaching response (Spooner, 1994) and so similar optical cross sections (σ). Thus, one can assume that all our samples have the same value of $\overline{\sigma\varphi_0}$ as determined above from the calibration sample. On the other hand, μ is a sample-dependent parameter that can vary from one rock to another. Accordingly, we simultaneously fit Eqn. 4 to all the profiles, sharing $\overline{\sigma\varphi_0}$ (2165±51 ka^{-1}, derived from the calibration sample) between all the fits, but leaving μ a free parameter.

Figure 5 shows the resulting best fits and the apparent luminescence surface-exposure ages for all the boulders. The corresponding values of μ are summarized in Table 1. The apparent luminescence age of sample MUST10-1 is 11.6±2.3 ka which is comparable with the ^{10}Be age of 9.9±0.9 ka obtained from the same surface (Fig. 5a). Also, boulder XJ64-1 has a minimum age of 36.4±2.1 ka constrained by our $1/\mu$ (mm) limit on the penetration depth of the $x_{50\%}$; this minimum age is consistent with the ^{10}Be age of 86.4±8.3 ka for this boulder (Fig. 5h). For all the other samples however, the apparent luminescence surface exposure ages are significantly younger than the corresponding ^{10}Be ages. This systematic underestimation in apparent luminescence exposure ages suggests that the profiles in these boulders are either in secular equilibrium or have been affected by erosion. To investigate this, a similar approach as was used with the calibration sample was adopted; we assume no erosion, and model two profiles for each sample by setting the exposure time to the ^{10}Be age of the sample or to infinity (Fig. 5).

As mentioned above, the apparent luminescence exposure age of sample MUST10-1 is comparable to its ^{10}Be age. As a result, the predicted profile corresponding to the ^{10}Be age in sample MUST10-1 is indistinguishable from the best fit of the model to the data, whereas the predicted secular-equilibrium profile is discernibly deeper (Fig. 5a). Also, in case of XJ64-1, the predicted steady-state and the fitted age model profiles are identical and deeper than the predicted ^{10}Be profile, indicating that this sample must be in secular equilibrium (Fig. 5h). Except for MUST10-1 and XJ64-1, the predicted ^{10}Be-equivalent and steady-state resetting profiles in all the other boulders penetrate to greater depths than the observed profiles, suggesting that the measured profiles are distinct and far from secular equilibrium; they must therefore have been affected by erosion (Fig. 5).

Given that erosion has most likely played a significant role in the development of the IRSL-depth profiles, we now test whether our data can be explained by the erosion rate model (Eqn. 8). As with Eqn. 4, we simultaneously fit Eqn. 8 to all the profiles, sharing $\overline{\sigma\varphi_0}$ (2165±51 ka^{-1}, derived from the calibration sample) between all the fits, but leaving μ a free parameter. Figure 5 shows that the model provides excellent fits to the data from all the samples; the fits are indistinguishable from and so superimpose those obtained using the age model (i.e. without erosion; Fig. 5). The resulting values of μ are summarized in Table 1. These are also indistinguishable from those derived using Eqn. 4 (Table 1); this is not surprising since μ is a material-dependent parameter and should not be dependent on age or erosion rate (see also Fig. S2 and associated text). The apparent erosion rates derived from Eqn. 8 vary from < 0.038±0.002 mm ka^{-1} for sample XJ64-1 to 444±12 mm ka^{-1} for sample XJ64 (Table 1).

6. Discussion

The apparent luminescence surface-exposure age of sample MUST10-1 is 11.6±2.3 ka which, within error limits, is in agreement with the ^{10}Be age of 9.9±0.9 ka obtained from the same surface (Fig. 5a). This is the first time that a luminescence surface exposure age has been verified using independent age control. Given that luminescence-depth profiles are much more susceptible to the effect of erosion than CN-depth profiles, the agreement between the two ages implies a low rate of erosion for the surface of this boulder. The application of the erosion rate model indeed confirms this implication, as it yields an apparent luminescence erosion rate of 0.09±0.02 mm ka^{-1} (Fig. 5a).

Boulder XJ64-1 with a ^{10}Be age of 86.4±8.3 ka has a minimum luminescence age of 36.4±2.1 ka (Fig. 5h). The fact that the observed profile is consistent with the expected profile in secular equilibrium assuming no erosion, suggests a negligible erosion of the surface of XJ64-1 (Fig. 5h). This suggestion is further confirmed by the application of erosion rate model, which results in a maximum apparent erosion rate of 0.038±0.002 mm ka^{-1} (Fig. 5h). The surface of boulder XJ64-1 currently lies only a few centimetres above the ground (Fig. 3h) and thus any effect of wind abrasion at its surface must be limited (Shao, 2009). The abundant desert varnish on the surface of this boulder (Fig. 3h) also argues for an absence of significant erosion, indicating that within the geological context, the very low erosion rate obtained here is plausible. Nevertheless, given the size and position of the boulder in the landscape, we cannot completely rule out occasional burial deep enough to shield it from daylight, but not from the cosmic rays. In such a scenario, the effective value of $\overline{\sigma\varphi_0}$ would be smaller than that for the calibration sample. However, any decrease in the effective $\overline{\sigma\varphi_0}$ value would only bring the equilibrium profile to depths shallower than we observe. Based on our fitting results we can conclude that the cover could have never been more than ~46% (minimum luminescence age/^{10}Be age) of the total time since the emplacement of the boulder.

In contrast to XJ64–1, the nearby large boulder (XJ64) has an anomalously high apparent erosion rate of 444±12 mm ka^{-1} (Fig. 5g), which is several orders of magnitude larger than those obtained for the other boulders in this study. The surface of XJ64 has visibly undergone considerable erosion compared to the other boulders, as evidenced by its rough, unvarnished surface (see also Fig. 3). Nevertheless, steady-state erosion at such a high rate seems very unlikely in an environment where it is expected that wind abrasion dominates (Portenga and Bierman, 2011). In addition, the boulder has been exposed for ~70 ka, and this would imply a loss of > 3 m, making the CN age a serious underestimate and the total loss even greater. A more likely explanation is that the observed profile was inadvertently sampled from a location where there had been a discrete loss of material, e.g. by freeze/thaw flaking.

We also note that the value of μ for this boulder (0.2 mm^{-1}) is ~3 times smaller than any of the values obtained for the other boulders, and this may reflect some undetected failure of the application of the model to this sample.

Finally, the observed marked variability in surface loss, as evidenced by apparent surface roughness in the field (Fig. 3), implies that the luminescence erosion rates derived here from such smooth varnished spots must be regarded as minimum estimates of rock surface erosion rates in the Eastern Pamirs, China. The observation of a significant varnish patina on surfaces probably eroding at > 0.1 to 2 mm ka^{-1} suggests that the varnish accumulation rates at the Eastern Pamirs must be higher than the fastest rates of ~600 μm ka^{-1} previously documented in southwestern United States (Spilde et al., 2013).

6.1. Luminescence-depth profile: chronometer or erosion-meter?

In order to discuss the information available in a luminescence-depth profile, we first simulate the behavior of the erosion rate model (Eqn. 8) for erosion rates of 0 and 1.5 mm ka^{-1}. The model profiles are first generated by setting t in Eqn. 4 to a known age (i.e. from 0.1 a to 100 ka) and then fitted by Eqn. (8) using the appropriate erosion rate. The other model parameters (i.e. $\dot{D}, D_o$, $\overline{\sigma\varphi_0}$ and μ) are assigned values comparable to those obtained for our samples. Figure 6a plots, against exposure time, the product of the $x_{50\%}$ of the resulting model profiles and μ; this gives a material independent, dimensionless parameter which quantifies the depth, in multiples of the mean free path, at which luminescence reaches 50% of its saturation value. We define the extrapolation of the horizontal (steady-state) part of the 1.5 mm ka^{-1} curve to the zero erosion rate curve to be the equilibrium age limit (i.e. ~1 ka) recorded by a profile eroding at 1.5 mm ka^{-1} (Fig. 6a). In a surface that has been exposed for a period much shorter than ~1 ka, the luminescence-depth profile is primarily a chronometer, because over this time span, the rate of migration of $x_{50\%}$ into the rock is much greater than the rate of removal of grains from the surface of the rock (Fig. 6a). Thus, a profile in this time zone can be fitted by Eqn. 4 to determine the apparent exposure age of the surface. On the other hand, at times much longer than the equilibrium age limit, the luminescence-depth profile is essentially an erosion-meter, because it is in erosional steady state and has no memory of the exposure time. A profile in this time zone can be modelled using Eqn. 8 to derive the erosion rate. There remains an intermediate transition interval (~0.3 to ~3 ka, points A and B in Fig. 6a) during which the luminescence-depth profile evolves from being a chronometer to an erosion-meter. In order to derive either the apparent exposure age or erosion rate in this transition period, a knowledge of the other parameter is required. In other words, to determine the apparent exposure age from a profile in this time zone, the erosion rate must be known independently, and vice versa.

In order to determine the equilibrium age range for various erosion rates, we have also simulated the behavior of the erosion rate model (Eqn. 8) for a range of erosion rates from 0 to 1500 mm ka^{-1}. In Figure 6b, the equilibrium ages for individual erosion rates are extrapolated onto the zero erosion rate curve. For the erosion rates relevant to our samples (0.015 to 1.5 mm ka^{-1}), luminescence-depth profiles reach equilibrium after 44 to 1 ka of exposure. These equilibrium age limits define the timescale to which the corresponding erosion rates refer. For instance, an erosion rate of 0.015 mm ka^{-1} is effectively averaged over the last 44 ka of surface exposure whereas an erosion rate of 1.5 mm ka^{-1} is only averaged over the last 1 ka. These luminescence-depth profiles have no memory of the erosion history prior to these age limits.

Depending on the parameter values and the depth resolution, the $1/\mu$ constraint can limit either the minimum apparent exposure age or the maximum apparent erosion rate that can be derived from a luminescence-depth profile. The typical value of μ in our samples is between 0.5 and 1 mm^{-1} (Fig. 5), meaning that the $x_{50\%}$ point in the deepest profiles that can be reliably distinguished from the bleaching/dose-rate steady-state profile must lie at least 1–2 mm shallower than the corresponding point in the steady-state profile. Given the current resolution of sampling (i.e. slicing at 1.5 mm depth intervals) and samples with typical parameter values, profiles with an apparent exposure age < 1 a or an apparent erosion rate > 1500 mm ka^{-1} (see Fig. 6) cannot be modelled reliably as these would be indistinguishable from steady-state. Collection of high-resolution data using spatially-resolved luminescence imaging techniques (e.g. Greilich and Wagner, 2006) may help to overcome this limitation in the future.

7. Conclusion

We have further developed the luminescence-surface exposure dating technique (Sohbati et al., 2012a,b) by taking the effect of rock surface erosion into account. The new model presented here (Eqn. 8) has been fitted to luminescence-depth profiles measured in subaerially exposed rock surfaces to give centennial- to millennial-scale (10^2–10^4 years) hard rock erosion rates. The model predicts that the higher the erosion rate, the faster a luminescence-depth profile changes from being a (surface exposure) chronometer to an erosion rate meter. For example, for an erosion rate of 1.5 mm ka^{-1} it takes only ~3 ka for a profile to become useful for deriving a unique erosion rate.

The application of the new model has been tested by fitting the IRSL-depth profiles measured into several glacial and landslide boulders in the Eastern Pamirs, China. The derived erosion rates for 7 out of the 8 boulders sampled in this study vary between < 0.038±0.002 and 1.72±0.04 mm ka^{-1} (the eighth boulder gave an anomalously high erosion rate, possibly due to a recent chipping/cracking loss of surface). In the case of one sample with a low erosion rate of 0.09±0.02 mm ka^{-1}, we obtained an apparent luminescence surface exposure age of 11.6±2.3 ka, consistent with the ^{10}Be age of 9.9±0.9 ka for the same surface. This is the first time that a luminescence surface exposure age has been verified by an independent age control.

Unfortunately, in the absence of an independent method that enables the measurement of erosion rates over similar timescales (i.e. 10^2–10^4 years), we cannot make any direct comparison between the rates measured here and those estimated using other techniques in the literature. It is however noteworthy that these luminescence erosion rates are only comparable with long-term CN erosion rates reported for the most-slowly eroding outcrops in polar climates with a median erosion rate of ~1 m Ma^{-1} (Portenga and Bierman, 2011). One can speculate that the lower centennial- to millennial-scale luminescence erosion rates derived here, when compared to the more typical CN rates measured in non-polar environments (Portenga and Bierman, 2011), may reflect the deceleration of erosion rates during the Holocene. However, any solid conclusion of this nature requires many more measurements of luminescence erosion rates in different environments and lithologies.

Acknowledgements

This work was financially supported by the Aarhus University Research Foundation (AUFF Pilotcenter for Quantitative Earth Surface Studies), the Carlsberg Foundation (Grant no. 2012_01_0838), the National Natural Science Foundation of China (Grant no.: 41472161), and the State Key Laboratory of Earthquake Dynamics (Grant no.: LED2013A09). BG was supported by the Netherlands Organisation for Scientific Research (NWO) VENI grant 863.15.026. We would like to thank Dr. Zhaode Yuan for providing us with his field photo of sample Muztagh–2. We thank Dr Nathan Brown for the careful review of the manuscript.

Appendix A

Consider Eqn. (7) from the main text:

$$\frac{dn}{dt} = (N-n)F - nE_0 e^{\mu\varepsilon t} \tag{7}$$

To solve Eqn. (7), we introduce $\tau = (\mu\varepsilon\,)^{-1}$ and make use of dimensionless variables $r = n/N$, $a = F\tau$ and $v = E(x(t))\tau = \tau E_0 \exp(t/\tau) = v_0 \exp\,(t/\tau)$, whose substitution into Eqn. (7) yields:

$$\frac{dr}{dt} = \frac{a}{\tau}(1-r) - \frac{v}{\tau}r \tag{A.1}$$

Dividing both sides of Eqn. (A.1) by the identity $dv/dt = v/\tau$ and rearranging results in:

$$\frac{dr}{dv} + r\left(\frac{a}{v} + 1\right) = \frac{a}{v} \tag{A.2}$$

Eq. (A.2) is a first order non-homogeneous differential equation. Recast as $dr/dv + f(r)r = g(r)$, it has a general solution $r = e^{-\int f(r)dx}\left\{\int e^{\int f(r)dx} g(r)dr + C\right\}$. Substituting $f(r) = a/v + 1,\ \ g(r) = a/v$, and integrating, we obtain:

$$r = av^{-a}e^{-v}\int_{v_0}^{v} u^{a-1}\, e^{u} du \tag{A.3}$$

where u is a dummy integration variable. To obtain an analytical solution for Eqn. (A.3), we start with the simple case of $v_0 = 0$ at $t = 0$, i.e. an initially negligible optical loss coefficient in Eqn. (7) in a mineral that is initially fully shielded from light. Using a power series to expand e^u in the integrand, we integrate and rearrange Eqn. (A.3) as follows:

$$r(v) = av^{-a}e^{-v}\int_0^v u^{a-1}\left(1+\frac{u}{1!}+\frac{u^2}{2!}+\cdots\right)du = av^{-a}e^{-v}\left(\frac{v^a}{a}+\frac{v^{a+1}}{(a+1)1!}+\frac{v^{a+2}}{(a+2)2!}+\cdots\right)$$

$$= e^{-v}\left(1+\frac{a}{(a+1)1!}v+\frac{a}{(a+2)2!}v^2+\cdots\right)$$

$$= e^{-v}\left(1+\frac{a}{(a+1)1!}v+\frac{a(a+1)}{(a+1)(a+2)2!}v^2+\cdots\right) \qquad (A.4)$$

Making the substitutions $z = v$, $m = a$ and $n = a + 1$, we notice that the power series in Eqn. (A.4) conforms to the confluent hypergeometric function (Abramowitz and Stegun, 1964):

$$M(m,n,z) = \left(1+\frac{m}{n\cdot 1!}z+\frac{m(m+1)}{n(n+1)2!}z^2+\cdots\right) \qquad (A.5)$$

which efficiently reduces Eqn. (A.4) to:

$$r(v) = e^{-v}M(a, a+1, v) \qquad (A.6)$$

To further simplify Eqn. (A. 6), we apply Kummer's theorem $M(m,n,z) = e^zM(n-m, n, -z)$, which reduces Eqn. (A.6) to the desired form:

$$r(v) = M(1, 1+a, -v) \qquad (A.7)$$

Remembering that $\tau = (\mu\varepsilon)^{-1}$, by substituting the dimensionless variables by physical variables, i.e. $r = n/N$, $a = F\tau$, and $v = E(x)\tau$ into Eqn. (A.7), for $x = x_0 - \varepsilon t$ we obtain:

$$\frac{n(x,\varepsilon)}{N} = M\left(1, 1+\frac{F}{\mu\varepsilon}, \frac{-E(x)}{\mu\varepsilon}\right) \qquad (A.8)$$

which is the same as Eqn. (8) in the main text, and describes luminescence systems exhuming towards the present-day surface from initially photon-impenetrable depths ($E_0 = 0$). The confluent hypergeometric function $M(m,n,z)$ is readily available in all common modelling software, either as an in-built function (e.g. Matlab, Mathematica) or as an optional extension (e.g. Excel, OriginLab). If nevertheless in need to numerically evaluate $M(m, n, z)$ using series expansion, consult Abramowitz and Stegun (1964).

The treatment can be further extended to include an arbitrary $E_0 \geq 0$, i.e. an initial boundary condition $0 \leq v0 < v$. To do this, we first expand Eqn. (A.3) into:

$$r = av^{-a}e^{-v}\int_{v_0}^{v} u^{a-1}\, e^{u} du = av^{-a}e^{-v}\int_{0}^{v} u^{a-1}\, e^{u} du - av^{-a}e^{-v}\int_{0}^{v_0} u^{a-1}\, e^{u} du \qquad (A.9)$$

We now use the previously-derived identity (Eqns. A.3 and A.7):

$$av^{-a}e^{-v}\int_{0}^{v} u^{a-1}\, e^{u} du = M(1, 1 + a, -v)$$

to express the last integral in Eqn. (A.9) as:

$$\int_{0}^{v_0} u^{a-1}\, e^{u} du = a^{-1}v_0^{a}e^{v_0}M(1, 1 + a, -v_0)$$

By substitution of the two identities above in to Eqn. (A.9), we obtain the desired form:

$$r(v) = M(1,1 + a, -v) - av^{-a}e^{-v}[a^{-1}v_0^{a}e^{v_0}M(1, 1 + a, -v_0)]$$

$$= M(1,1 + a, -v) - (v_0/v)^{\,a}\, e^{v_0 - v}\, M(1, 1 + a, -v_0) \qquad (A.10)$$

References

Abramowitz, M., Stegun, I., 1964. Handbook of mathematical functions: with formulas, graphs, and mathematical tables. Vol. 55. Courier Corporation.

Aitken, M.J., 1985. Thermoluminescence dating, Studies in Archaeological Science.

Aitken, M.J., 1998. An introduction to optical dating: The dating of Quaternary sediments by the use of photon-stimulated luminescence, Oxford science publications. doi:10.1002/(SICI)1520-6548(200001)15:1<81::AID-GEA5>3.3.CO;2-Y

Balco, G., Stone, J.O., Lifton, N.A., Dunai, T.J., Lifton, A., Dunai, T.J., 2008. A complete and easily accessible means of calculating surface exposure ages or erosion rates from 10Be and 26Al measurements. Quat. Geochronol. 3, 174–195. doi:10.1016/j.quageo.2007.12.001

Baril, M.R., Huntley, D.J., 2003. Infrared stimulated luminescence and phosphorescence spectra of irradiated feldspars. J. Phys. Condens. Matter 15, 8029–8048. doi:10.1088/0953-8984/15/46/018

Borchers, B., Marrero, S., Balco, G., Caffee, M., Goehring, B., Lifton, N., Nishiizumi, K., Phillips, F., Schaefer, J., Stone, J., 2016. Geological calibration of spallation production rates in the CRONUS-Earth project. Quat. Geochronol. 31, 188–198. doi:10.1016/j.quageo.2015.01.009

Braun, J., Van Der Beek, P., Batt, G., 2006. Quantitative thermochronology: numerical methods for the interpretation of thermochronological data. Cambridge University Press.

Gardner, T.W., Jorgensen, D.W., Shuman, C., Lemieux, C.R., 1987. Geomorphic and tectonic process rates: effects of measured time interval. Geology 15, 259–261. doi:10.1130/0091-7613(1987)15<259:GATPRE>2.0.CO

Greilich, S., Wagner, G.A., 2006. Development of a spatially resolved dating technique using HR-OSL. Radiat. Meas. 41, 738–743. doi:10.1016/j.radmeas.2006.05.022

Guérin, G., Mercier, N., Adamiec, G., 2011. Dose-rate conversion factors: update. Anc. TL 29, 5–8.

Guralnik, B., Jain, M., Herman, F., Paris, R.B., Harrison, T.M., Murray, A.S., Valla, P.G., Rhodes, E.J., 2013. Effective closure temperature in leaky and/or saturating thermochronometers. Earth Planet. Sci. Lett. 384, 209–218. doi:10.1016/j.epsl.2013.10.003

Guralnik, B., Ankjærgaard, C., Jain, M., Murray, A.S., Müller, a., Wälle, M., Lowick, S.E., Preusser, F., Rhodes, E.J., Wu, T.-S., Mathew, G., Herman, F., 2015. OSL-thermochronometry using bedrock quartz: A note of caution. Quat. Geochronol. 25, 37–48. doi:10.1016/j.quageo.2014.09.001

Habermann, J., Schilles, T., Kalchgruber, R., Wagner, G.A., 2000. Steps towards surface dating using luminescence. Radiat. Meas. 32, 847–851. doi:10.1016/S1350-4487(00)00066-4

Huntley, D.J., Hancock, G.V., 2001. The Rb contents of the K-feldspar grains being measured in optical dating. Anc. TL 19, 43–46.

Huntley, D.J., 2006. An explanation of the power-law decay of luminescence. J. Phys. Condens. Matter 18, 1359–1365. doi:10.1088/0953-8984/18/4/020

Kirchner, J.W., Finkel, R.C., Riebe, C.S., Granger, D.E., Clayton, J.L., King, J.G., Megahan, W.F., Sites, F., 2001. Mountain erosion over 10 yr, 10 k.y., and 10 m.y. time scales. Geology 29, 591–594. doi:10.1130/0091-7613(2001)029<0591:MEOYKY>2.0.CO;2

Koppes, M.N., Montgomery, D.R., 2009. The relative efficacy of fluvial and glacial erosion over modern to orogenic timescales. Nat. Geosci. 2, 644–647. doi:10.1038/ngeo616

Lal, D., 1991. Cosmic ray labeling of erosion surfaces: in situ nuclide production rates and erosion models. Earth Planet. Sci. Lett. 104, 424–439. doi:10.1016/0012-821X(91)90220-C

Lal, D., Gallup, C.D., Somayajulu, B.L.K., Vacher, L., Caffee, M.W., Jull, A.J.T., Finkel, R.C., Speed, R.C., Winter, A., 2005. Records of cosmogenic radionuclides ^{10}Be, ^{26}Al and ^{36}Cl in corals: First studies on coral erosion rates and potential of dating very old corals. Geochim. Cosmochim. Acta 69, 5717–5728. doi:10.1016/j.gca.2005.08.012

Lamothe, M., Auclair, M., Hamzaoui, C., Huot, S., 2003. Towards a prediction of long-term anomalous fading of feldspar IRSL. Radiat. Meas. 37, 493–498. doi:10.1016/S1350-4487(03)00016-7

Laskaris, N., Liritzis, I., 2011. A new mathematical approximation of sunlight attenuation in rocks for surface luminescence dating. J. Lumin. 131, 1874–1884. doi:10.1016/j.jlumin.2011.04.052

Lehmann, B., Valla, P.G., King, G.E., Herman, F., 2018. Investigation of OSL surface exposure dating to reconstruct post-LIA glacier fluctuations in the French Alps (Mer de Glace, Mont Blanc massif). Quat. Geochronol. 44, 63–74. doi:10.1016/j.quageo.2017.12.002

Liu, J., Sohbati, R., Murray, A.S., Jain, M., Andersen, J.L., Egholm, D.L., Linge, H., Chen, J., Luo, M., Zheng, R., in review. Luminescence rock-surface dating reveals complex depositional histories of glacial and landslide boulders. Earth Planet. Sci. Lett.

Mejdahl, V., 1987. Internal radioactivity in quartz and feldspar grains. Anc. TL 5, 10–17.

Moses, C., Robinson, D., Barlow, J., 2014. Methods for measuring rock surface weathering and erosion: A critical review. Earth-Science Rev. 135, 141–161. doi:10.1016/j.earscirev.2014.04.006

Murray, A.S., Marten, R., Johnson, A., Martin, P., 1987. Analysis for naturally-occurring radionuclides at environmental concentrations by gamma spectrometry. J. Radioanal. Nucl. Chem. 115, 263–288.

Nishiizumi, K., Lal, D., Klein, J., Middleton, R., Arnold, J., 1986. Production of ^{10}Be and ^{26}Al by cosmic rays in terrestrial quartz in–situ and implications for erosion rates. Nature 319, 134–136. doi:http://dx.doi.org/10.1038/319134a0

Owen, L.A., Chen, J., Hedrick, K.A., Caffee, M.W., Robinson, A.C., Schoenbohm, L.M., Yuan, Z., Li, W., Imrecke, D.B., Liu, J., 2012. Quaternary glaciation of the Tashkurgan Valley, Southeast Pamir. Quat. Sci. Rev. 47, 56–72. doi:10.1016/j.quascirev.2012.04.027

Pederson, J.L., Chapot, M.S., Simms, S.R., Sohbati, R., Rittenour, T.M., Murray, A.S., Cox, G., 2014. Reply to Simon and Reed: Independent and converging results rule out historic disturbance and confirm age constraints for Barrier Canyon rock art. Proc. Natl. Acad. Sci. 111, E5604–E5604. doi:10.1073/pnas.1421319112

Portenga, E.W., Bierman, P.R., 2011. Understanding earth's eroding surface with ^{10}Be. GSA Today 21, 4–10. doi:10.1130/G111A.1

Prescott, J.R., Hutton, J.T., 1994. Cosmic ray contributions to does rates for Luminescence and ESR dating: large depths and long-terms variations. Radiat. Meas. 23, 497–500.

Sanderson, D., Smillie, M., McCullagh, R., Feathers, J., Hauser, N., 2011. Surface exposure dating by luminescence: developing and testing models for surface bleaching rates and erosion rates. 13th International Conference on Luminescence and Electron Spin Resonance Dating, 10-14 July 2011, Toruń, Poland, Book of Abstracts, p. 178.

Schumm, S.A., Lichty, R.W., 1965. Time, space, and causality in geomorphology. Am. J. Sci. doi:10.2475/ajs.263.2.110

Seong, Y.B., Owen, L.A., Yi, C., Finkel, R.C., 2009a. Quaternary glaciation of Muztag Ata and Kongur Shan: Evidence for glacier response to rapid climate changes throughout the late glacial and holocene in westernmost Tibet. Bull. Geol. Soc. Am. 121, 348–365. doi:10.1130/B26339.1

Seong, Y.B., Owen, L. A., Yi, C., Finkel, R.C., Schoenbohm, L., 2009b. Geomorphology of anomalously high glaciated mountains at the northwestern end of Tibet: Muztag Ata and Kongur Shan. Geomorphology 103, 227–250. doi:10.1016/j.geomorph.2008.04.025

Shao, Y., 2009. Physics and Modelling of Wind Erosion, Physics and Modelling of Wind Erosion. Springer Netherlands, Dordrecht. doi:10.1007/978-1-4020-8895-7_4

Sohbati, R., Murray, A.S., Jain, M., Buylaert, J.-P., Thomsen, K.J., 2011. Investigating the resetting of OSL signals in rock surfaces. Geochronometria 38, 249–258. doi:10.2478/s13386-011-0029-2

Sohbati, R., Murray, A.S., Chapot, M.S., Jain, M., Pederson, J., 2012a. Optically stimulated luminescence (OSL) as a chronometer for surface exposure dating. J. Geophys. Res. 117, B09202. doi:10.1029/2012JB009383

Sohbati, R., Jain, M., Murray, A., 2012b. Surface exposure dating of non-terrestrial bodies using optically stimulated luminescence: A new method. Icarus 221, 160–166.

Sohbati, R., Murray, A.S., Buylaert, J.-P., Almeida, N. A. C., Cunha, P.P., 2012c. Optically stimulated luminescence (OSL) dating of quartzite cobbles from the Tapada do Montinho archaeological site (east-central Portugal). Boreas 41, 452–462. doi:10.1111/j.1502-3885.2012.00249.x

Sohbati, R., Murray, A.S., Porat, N., Jain, M., Avner, U., 2015. Age of a prehistoric “Rodedian” cult site constrained by sediment and rock surface luminescence dating techniques. Quat. Geochronol. 30, 90–99. doi:10.1016/j.quageo.2015.09.002

Spilde, M.N., Melim, L.A., Northup, D.E., Boston, P.J., 2013. Anthropogenic lead as a tracer of rock varnish growth: Implications for rates of formation. Geology 41, 263–266. doi:10.1130/G33514.1

Stone, J.O., 2000. Air pressure and cosmogenic isotope production. J. Geophys. Res. 105759, 753–23. doi:10.1029/2000JB900181

Stephenson, W.J., Finlayson, B.L., 2009. Measuring erosion with the micro-erosion meter—Contributions to understanding landform evolution. Earth-Science Rev. 95, 53–62. doi:10.1016/j.earscirev.2009.03.006

Turowski, J.M., Cook, K.L., 2017. Field techniques for measuring bedrock erosion and denudation. Earth Surf. Process. Landforms 42, 109–127. doi:10.1002/esp.4007

Xu, X., Yi, C., 2014. Little Ice Age on the Tibetan Plateau and its bordering mountains: Evidence from moraine chronologies. Glob. Planet. Change 116, 41–53. doi:10.1016/j.gloplacha.2014.02.003

Yuan, Z., Chen, J., Owen, L.A., Hedrick, K.A., Caffee, M.W., Li, W., Schoenbohm, L.M., Robinson, A.C., 2013. Nature and timing of large landslides within an active orogen, eastern Pamir, China. Geomorphology 182, 49–65. doi:10.1016/j.geomorph.2012.10.028

Viles, H.A., 2001. Scale issues in weathering studies. Geomorphology 41, 63–72. doi:10.1016/S0169-555X(01)00104-0

Wallinga, J., Murray, A., Wintle, A., 2000. The single-aliquot regenerative-dose (SAR) protocol applied to coarse-grain feldspar. Radiat. Meas. 32, 529–533. doi:10.1016/S1350-4487(00)00091-3

Wallinga, J., Bos, A.J.J., Dorenbos, P., Murray, A.S., Schokker, J., 2007. A test case for anomalous fading correction in IRSL dating. Quat. Geochronol. 2, 216–221. doi:10.1016/j.quageo.2006.05.014

Warke, P.A., McKinley, J.M., 2011. Scale issues in geomorphology. Geomorphology 130, 1–4. doi:10.1016/j.geomorph.2011.04.031

Wintle, A., Murray, A.S., 2006. A review of quartz optically stimulated luminescence characteristics and their relevance in single-aliquot regeneration dating protocols. Radiat. Meas. 41, 369–391. doi:10.1016/j.radmeas.2005.11.001

Figure captions

Figure 1) Model luminescence-depth profiles as predicted by Eqns (4) and (8) for (a) a non-eroding and (b) an eroding rock surface, respectively. The selected parameter values are $\dot{D}$ = 6 Gy ka^{-1}, D_o = 250 Gy, $\overline{\sigma\varphi_0}$ = 2200 ka^{-1} and μ = 0.6 mm^{-1} comparable to the average values obtained for the samples used in this study.

Figure 2) Study area and sampling sites, Southeast Pamir, China. Glacial and landslide boulders were resampled from three different sites along the Tashkurgan valley. The age ranges represent the ^{10}Be ages of boulder surfaces previously determined by Seong et al. (2009a) (8–9 ka), Yuan et al. (2013) (14–15 ka) and Owen et al. (2012) (65–87 ka).

Figure 3) View of the boulders sampled for this study. The red arrows point to the sample locations.

Figure 4) (a) View of Muztagh–2 ^{10}Be sample previously taken by Yuan et al. (2013) in 2010. (b) View of the same sample as in (a) sampled in 2013 as non-eroding known-age sample for calibration of luminescence-depth profiles. (c) Variation of the normalized natural sensitivity-corrected IRSL residual signal (L_n/T_n) with depth into i) the bottom of a > 2-cm deep chiseled surface where Muztagh–2 ^{10}Be sample had been collected (red circles), and ii) the natural varnished surface of the boulder (black circles). Each data point represents the signal measured from at least one whole rock slice coming from a certain depth into the boulder and thus represents the average luminescence at that depth. The error bars represent one standard error. For normalization, the L_n/T_n value of each slice was divided by the average of saturated L_n/T_n values measured from depths > 20 mm (i.e. depths in field saturation) in the corresponding profile. The solid lines show the best simultaneous fits to both data sets using Eqn. 4 with the surface bleaching rate $\overline{\sigma\varphi_0}$ and the light attenuation coefficient μ as shared parameters between the two fits. The fittings were done using Poisson weighting ($w_i = 1/y_i$).

Figure 5) Variation of the normalized natural sensitivity-corrected IRSL signal (L_n/T_n) with depth in all samples. Each data point is an average of the residual signal measured from at least three intact rock slices of the same depth coming from parallel cores (< 5 cm apart) drilled into the same surface. The error bars represent one standard error. The normalization factor was obtained by averaging the L_n/T_n values at depths > 20 mm (i.e. depths in field saturation) for individual profiles. The visually-indistinguishable overlapping solid lines indicate the best fits of Eqns. 4 and 8 to the data points, resulting in the apparent luminescence surface-exposure age and erosion rate as model parameters. $\overline{\sigma\varphi_0}$ was set to 2165 ka^{-1} as the shared parameter value between all the fits and μ was free to float as the sample-dependent parameter. $\dot{D}$ and D_o had the same values as in Table 1. The fittings were performed using Poisson weighting ($w_i = 1/y_i$). The dashed and dotted lines represent erosion-free model profiles obtained by replacing the time in Eqn. 4 with (i) the ^{10}Be age of the same surface and (ii) infinity.

Figure 6) The model dependence of luminescence-depth profiles on erosion rate and exposure time. (a) Profiles generated by setting t in Eqn. 4 to a particular age (from 0.1 a to 100 ka) and then fitting these modelled profiles with Eqn. (8) using erosion rates of 0 and 1.5 mm ka^{-1}. The equilibrium age limit (see text) is indicated by the extrapolation of the steady-state part of the 1.5 mm ka^{-1} curve onto the zero erosion rate curve. The transition zone between the time ranges in which the profile eroding at 1.5 mm ka^{-1} acts as chronometer or an erosion-meter is indicated by the points A and B arbitrarily defined to lie 10% within the chronometer and erosion-meter parts of the 1.5-mm ka^{-1} curve, respectively. (b) Modelled profiles generated as in (a) but using different erosion rates between 0 and 1500 mm ka^{-1}, showing their respective equilibrium ages on the zero erosion rate curve.

Table captions

Table 1) Summary of samples, model parameter values, luminescence surface-exposure ages and erosion rates. All the ^{10}Be ages were calculated using the CRONUS online calculator version 2.3 (Balco et al., 2008) with high latitude/sea level production rate of 4.01 (Borcher et al., 2016), assuming standard atmosphere, zero erosion and the time-dependent Lal/Stone (2000) spallation scaling scheme, and are normalized to the “07KNSTD” isotope ratio standardization. The uncertainties include errors associated with scaling and calibration (external uncertainty).

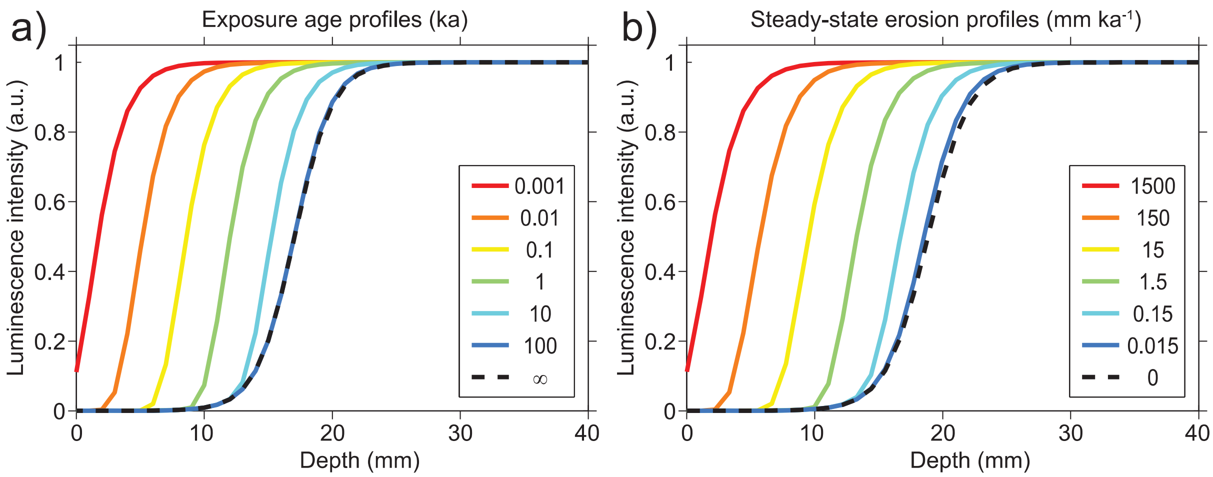
a)
Exposure age profiles (ka)
Luminescence intensity (a.u.)
Depth (mm)
0.001
0.01
0.1
1
10
100
∞
b)
Steady-state erosion profiles (mm ka-1)
Luminescence intensity (a.u.)
Depth (mm)
1500
150
15
1.5
0.15
0.015
0

728 **Figure 1)**

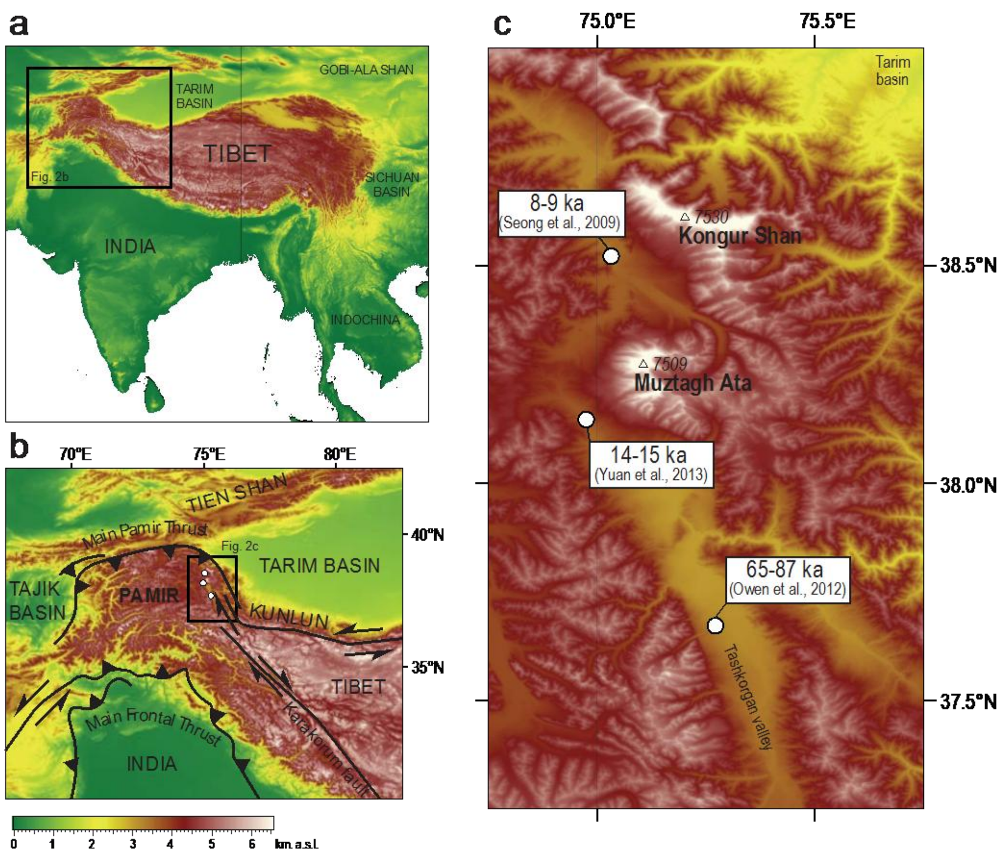
a
GOBI-ALA SHAN
TARIM BASIN
TIBET
Fig. 2b
SICHUAN BASIN
INDIA
INDOCHINA
b
70°E
75°E
80°E
TIEN SHAN
Main Pamir Thrust
Fig. 2c
TARIM BASIN
40°N
TAJIK BASIN
PAMIR
KUNLUN
35°N
TIBET
Main Frontal Thrust
Karakorum fault
INDIA
0 1 2 3 4 5 6 km a.s.l.
c
75.0°E
75.5°E
Tarim basin
8-9 ka
(Seong et al., 2009)
7530
Kongur Shan
38.5°N
7509
Muztagh Ata
14-15 ka
(Yuan et al., 2013)
38.0°N
65-87 ka
(Owen et al., 2012)
Tashkorgan valley
37.5°N

Figure 2)

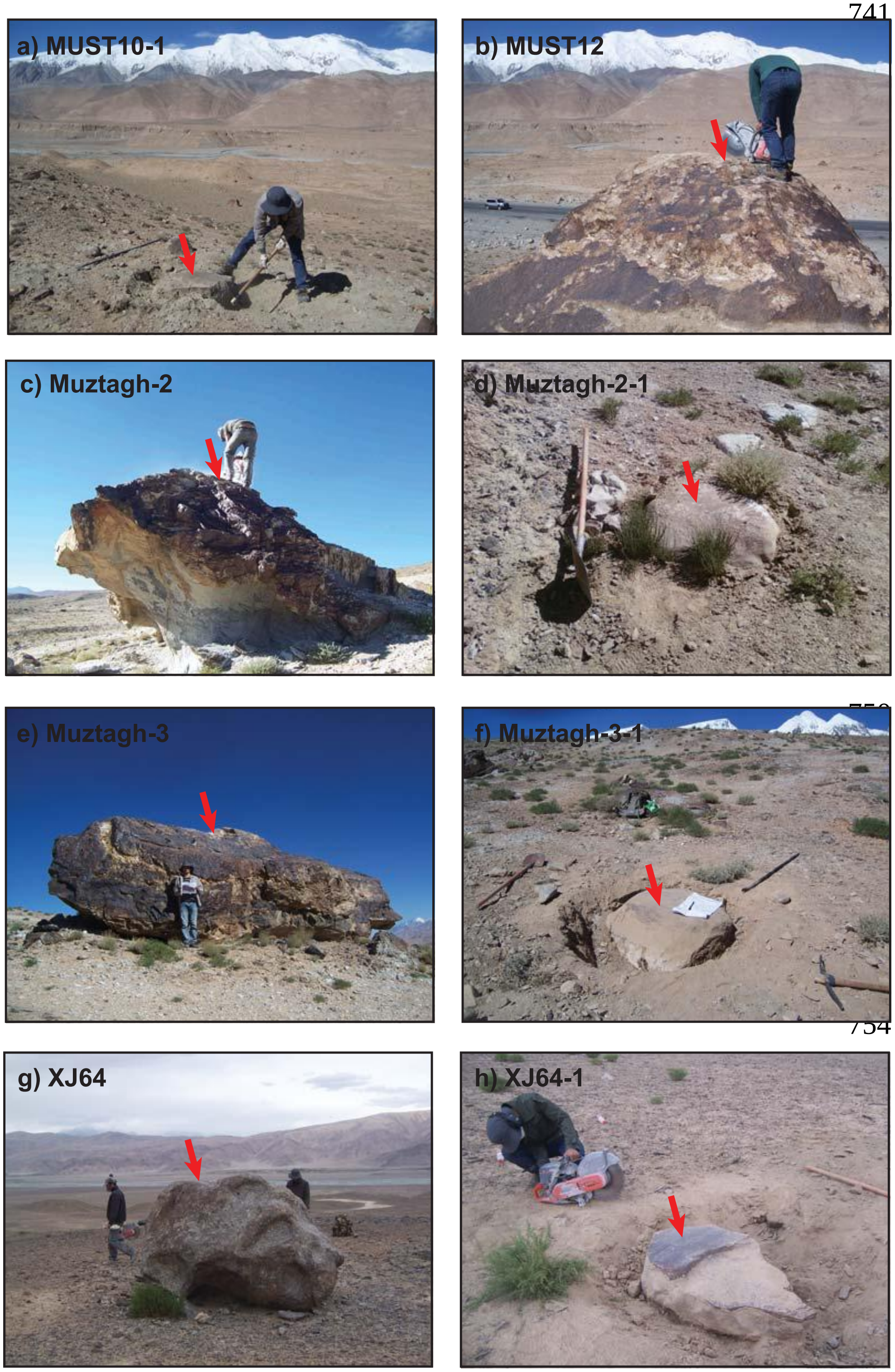
a) MUST10-1
b) MUST12
c) Muztagh-2
d) Muztagh-2-1
e) Muztagh-3
f) Muztagh-3-1
g) XJ64
h) XJ64-1

Figure 3)

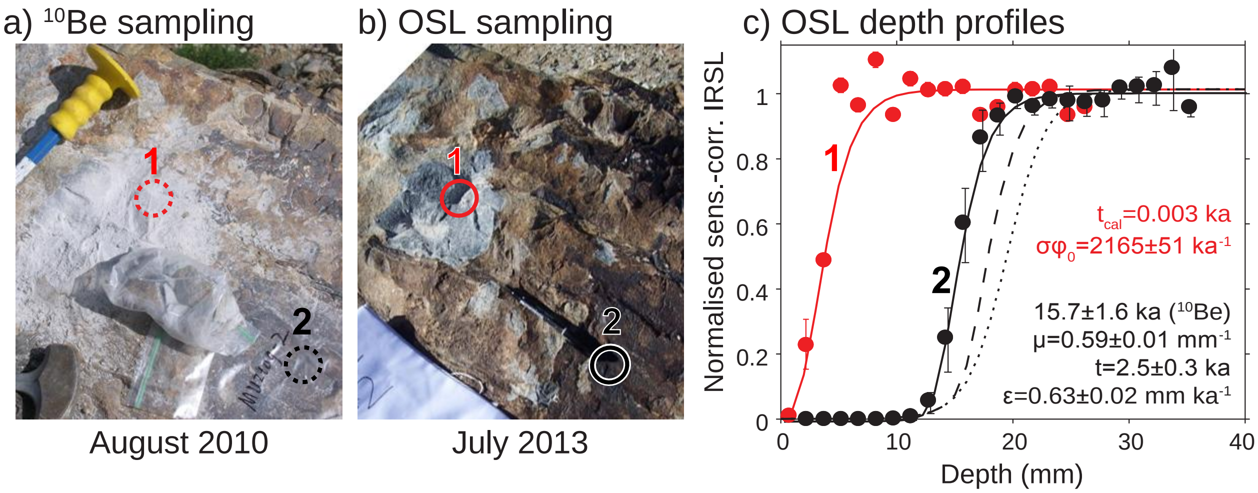
a) ^{10}Be sampling
1
2
August 2010
b) OSL sampling
1
2
July 2013
c) OSL depth profiles
Normalised sens.-corr. IRSL
0
0.2
0.4
0.6
0.8
1
0
10
20
30
40
Depth (mm)
1
2
t_{cal}=0.003 ka
$\sigma\varphi_0$=2165±51 ka^{-1}
15.7±1.6 ka (^{10}Be)
μ=0.59±0.01 mm^{-1}
t=2.5±0.3 ka
ε=0.63±0.02 mm ka^{-1}

Figure 4)

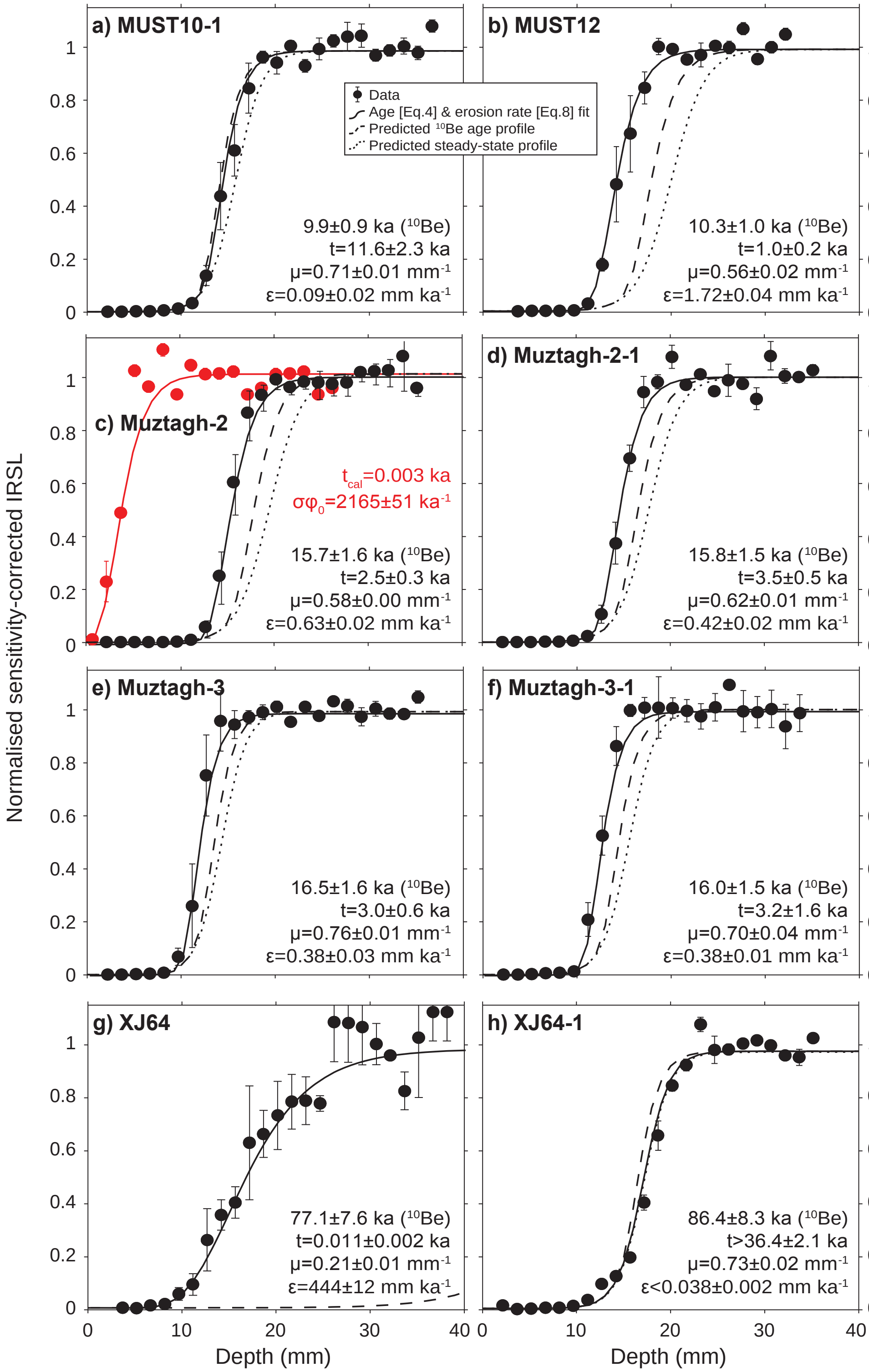

a) MUST10-1
b) MUST12
c) Muztagh-2
d) Muztagh-2-1
e) Muztagh-3
f) Muztagh-3-1
g) XJ64
h) XJ64-1
Data
Age [Eq.4] & erosion rate [Eq.8] fit
Predicted ¹⁰Be age profile
Predicted steady-state profile
9.9±0.9 ka (¹⁰Be)
t=11.6±2.3 ka
μ=0.71±0.01 mm⁻¹
ε=0.09±0.02 mm ka⁻¹
10.3±1.0 ka (¹⁰Be)
t=1.0±0.2 ka
μ=0.56±0.02 mm⁻¹
ε=1.72±0.04 mm ka⁻¹
t_cal=0.003 ka
σφ₀=2165±51 ka⁻¹
15.7±1.6 ka (¹⁰Be)
t=2.5±0.3 ka
μ=0.58±0.00 mm⁻¹
ε=0.63±0.02 mm ka⁻¹
15.8±1.5 ka (¹⁰Be)
t=3.5±0.5 ka
μ=0.62±0.01 mm⁻¹
ε=0.42±0.02 mm ka⁻¹
16.5±1.6 ka (¹⁰Be)
t=3.0±0.6 ka
μ=0.76±0.01 mm⁻¹
ε=0.38±0.03 mm ka⁻¹
16.0±1.5 ka (¹⁰Be)
t=3.2±1.6 ka
μ=0.70±0.04 mm⁻¹
ε=0.38±0.01 mm ka⁻¹
77.1±7.6 ka (¹⁰Be)
t=0.011±0.002 ka
μ=0.21±0.01 mm⁻¹
ε=444±12 mm ka⁻¹
86.4±8.3 ka (¹⁰Be)
t>36.4±2.1 ka
μ=0.73±0.02 mm⁻¹
ε<0.038±0.002 mm ka⁻¹
Normalised sensitivity-corrected IRSL
Depth (mm)

Figure 5)

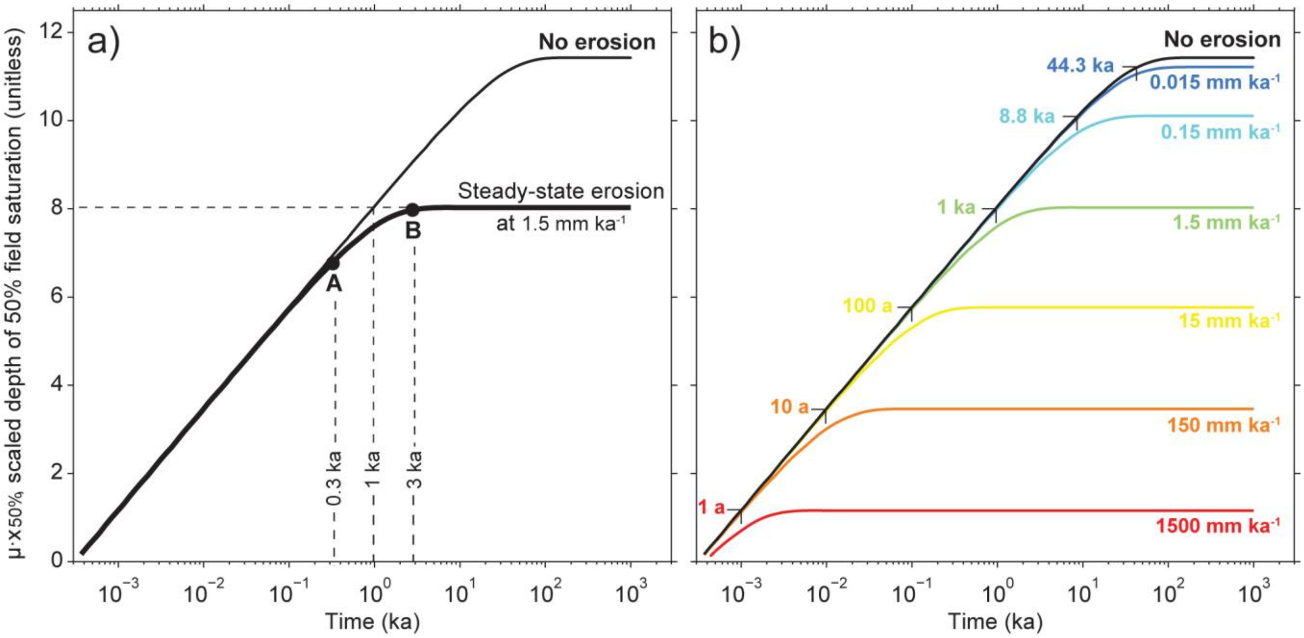

a)
No erosion
Steady-state erosion
at 1.5 mm ka-1
A
B
0.3 ka
1 ka
3 ka
µ·x50% scaled depth of 50% field saturation (unitless)
Time (ka)
b)
No erosion
44.3 ka
0.015 mm ka-1
8.8 ka
0.15 mm ka-1
1 ka
1.5 mm ka-1
100 a
15 mm ka-1
10 a
150 mm ka-1
1 a
1500 mm ka-1
Time (ka)

Figure 6)

Sample name	Landform	Lithology	$\dot{D}$	D_0	Age model		Erosion rate model		Published ^{10}Be age[*]	^{10}Be age Reference
					μ	age	μ	erosion rate		
			(Gy ka^{-1})	(Gy)	mm^{-1}	ka	mm^{-1}	mm ka^{-1}	ka	
			± se	± se	± se	± se	± se	± se	± se	
MUST10–1	Moraine	Granite gneiss	7.99±0.14	276±23	0.71±0.01	11.6±2.3	0.71±0.01	0.09±0.02	9.9±0.9	Liu et al. (in review)
MUST12	Moraine	Granite gneiss	6.98±0.15	264±7	0.56±0.02	1.0±0.2	0.56±0.02	1.72±0.04	10.3±1.0[*]	Seong et al. (2009a)
MUZTAGH–2	Landslide	Granite gneiss	5.45±0.09	238±34	0.59±0.01	2.5±0.3	0.58±0.00	0.63±0.02	15.7±1.6[*]	Yuan et al. (2013)
MUZTAGH–2–1	Landslide	Granite gneiss	6.49±0.10	214±16	0.63±0.01	3.5±0.5	0.62±0.01	0.42±0.02	15.8±1.5	Liu et al. (in review)
MUZTAGH–3	Landslide	Granite gneiss	6.19±0.11	176±12	0.77±0.01	3.0±0.6	0.76±0.01	0.38±0.03	16.5±1.6[*]	Yuan et al. (2013)
MUZTAGH–3–1	Landslide	Granite gneiss	6.23±0.11	225±13	0.73±0.03	3.2±1.6	0.70±0.04	0.38±0.01	16.0±1.5	Liu et al. (in review)
XJ64	Moraine	Granodiorite	7.33±0.15	245±18[**]	0.21±0.01	0.011±0.002	0.21±0.01	444±12	77.1±7.6[*]	Owen et al. (2012)
XJ64–1	Moraine	Quartzite	2.72±0.06	320±12	0.73±0.02	>36.4±2.1	0.73±0.02	<0.038±0.002	86.4±8.3	Liu et al. (in review)

[*] The age was recalculated for consistency with those in Liu et al. (in review).

[**] No D_o was measured for this sample. This is an average of the D_0 values measured for the other samples.

Table 1)

Supplementary material

Sample Name	^{238}U	^{226}Ra	^{232}Th	^{40}K	Beta dose rate	Gamma dose rate	Mean K-felds grain size
	(Bq kg^{-1}) ± se	(Bq kg^{-1}) ± se	(Bq kg^{-1}) ± se	(Bq kg^{-1}) ± se	(Gy ka^{-1}) ± se	(Gy ka^{-1}) ± se	µm
MUST10–1	73±9	109.1±1.2	146.2±1.2	1274±22	3.39±0.06	3.48±0.09	800
MUST12	34±12	31±1	58.7±1	1469±27	2.58±0.05	2.06±0.03	1000
MUZTAGH–2	48±12	34±1	77.9±1.2	931±21	2.68±0.06	1.89±0.03	400
MUZTAGH–2–1	27±8	32±0.7	97.5±1.1	1230±22	3.00±0.05	2.34±0.03	600
MUZTAGH–3	65±11	112.8±1.4	109.7±1.3	750±17	2.99±0.07	2.66±0.09	400
MUZTAGH–3–1	45±9	49±0.8	91.9±1.2	1061±21	2.79±0.05	2.26±0.05	600
XJ64	52±9	66±1	91.5±1.2	1229±24	2.51±0.04	2.51±0.06	1000
XJ64–1	24±7	19.5±0.6	23.2±0.7	366±10	1.19±0.04	0.70±0.02	150

Table S1) Summary of radionuclide concentrations, infinite matrix beta and gamma dose rates and K-feldspar grain sizes as used in the calculation of total effective dose rate.

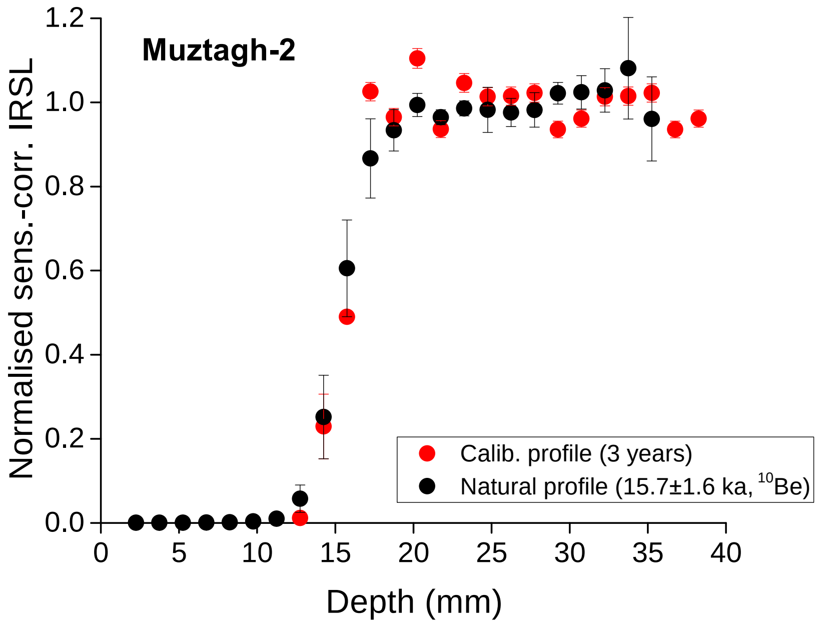

Fig. S1) The 3-year old calibration profile (profile 1, Fig. 4c) superimposed on the natural profile (profile 2, Fig. 4c) by adding 12 mm to the depths of profile 1. The two profiles are indistinguishable, confirming that any effect of signal instability on the shape of the profile is negligible over a timescale of up to ~16 ka.

Sensitivity of the fitted value of μ to erosion rate (ε) and exposure time (t)?

In order to investigate the possible effect of erosion on μ, we numerically simulated profiles, using Eqns. (1), (2), (3) and (5), for a range of erosion rates from 0 to 5 mm ka^{-1} over a wide range of exposure times from 1 a to 100 ka. We then fitted the resulting modelled profiles with Eqn. (4) to determine the best-fit value for μ (Fig. S2). The variation in the resulting value of μ obtained using the age model (i.e. no erosion) when fitted to these simulated profiles affected by erosion is < 0.5% around the true value over an exposure time of up to 100 ka.

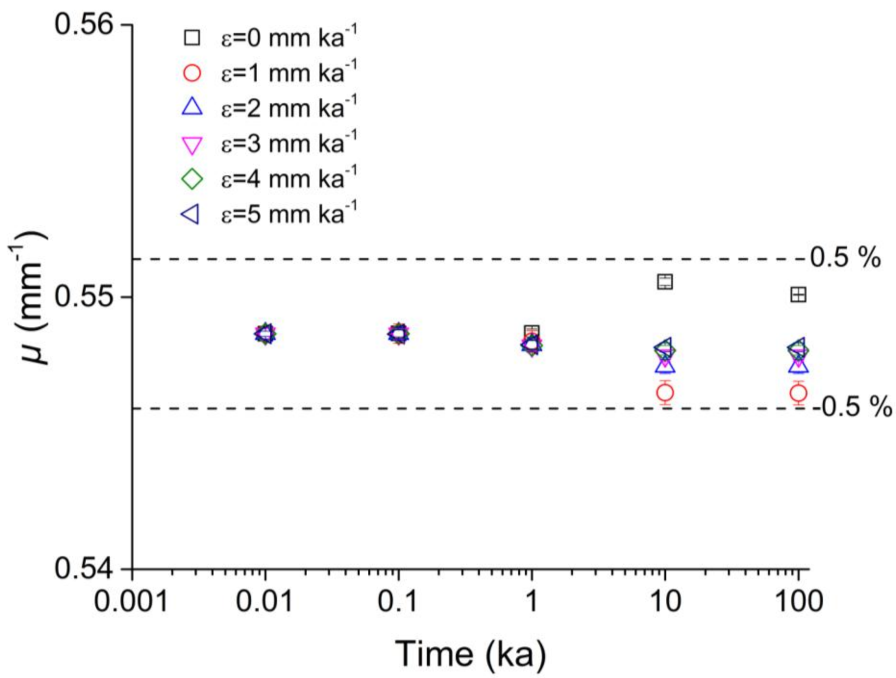

Fig. S2) Dependence of fitted μ on apparent age and erosion rate using numerically simulated data.